ACS APPLIED MATERIALS & INTERFACES

www.acsami.org

Research Article

Chemosensitization of Temozolomide-Resistant Pediatric Diffuse Midline Glioma Using Potent Nanoencapsulated Forms of a N(3)-Propargyl Analogue

Vahid Heravi Shargh, Jeni Luckett, Kaouthar Bouzinab, Stephen Paisey, Lyudmila Turyanska, William G. B. Singleton, Stephen Lowis, Pavel Gershkovich, Tracey D. Bradshaw, Malcolm F. G. Stevens, Alison Bienemann, and Beth Coyle*

Cite This: https://doi.org/10.1021/acsami.1c04164

Read Online

ACCESS | Metrics & More | Article Recommendations | Supporting Information

ABSTRACT: Abstract: The lack of clinical response to the alkylating agent temozolomide (TMZ) in pediatric diffuse midline/intrinsic pontine glioma (DIPG) has been associated with O^6-methylguanine-DNA-methyltransferase (MGMT) expression and mismatch repair deficiency. Hence, a potent N(3)-propargyl analogue (N3P) was derived, which not only evades MGMT but also remains effective in mismatch repair deficient cells. Due to the poor pharmacokinetic profile of N3P ($t_{1/2}$ < 1 h) and to bypass the blood−brain barrier, we proposed convection enhanced delivery (CED) as a method of administration to decrease dose and systemic toxicity. Moreover, to enhance N3P solubility, stability, and sustained distribution *in vivo*, either it was incorporated into an apoferritin (AFt) nanocage or its sulfobutyl ether β-cyclodextrin complex was loaded into nanoliposomes (Lip). The resultant AFt-N3P and Lip-N3P nanoparticles (NPs) had hydrodynamic diameters of 14 *vs* 93 nm, icosahedral *vs* spherical morphology, negative surface charge (−17 *vs* −34 mV), and encapsulating ∼630 *vs* ∼21000 N3P molecules per NP, respectively. Both NPs showed a sustained release profile and instant uptake within 1 h incubation *in vitro*. In comparison to the naked drug, N3P NPs demonstrated stronger anticancer efficacy against 2D TMZ-resistant DIPG cell cultures [IC_{50} = 14.6 (Lip-N3P) *vs* 32.8 μM (N3P); DIPG-IV) and (IC_{50} = 101.8 (AFt-N3P) *vs* 111.9 μM (N3P); DIPG-VI)]. Likewise, both N3P-NPs significantly (P < 0.01) inhibited 3D spheroid growth compared to the native N3P in $MGMT^+$ DIPG-VI (100 μM) and mismatch repair deficient DIPG-XIX (50 μM) cultures. Interestingly, the potency of TMZ was remarkably enhanced when encapsulated in AFt NPs against DIPG-IV, -VI, and -XIX spheroid cultures. Dynamic PET scans of CED-administered zirconium-89 (^{89}Zr)-labeled AFt-NPs in rats also demonstrated substantial enhancement over free ^{89}Zr radionuclide in terms of localized distribution kinetics and retention within the brain parenchyma. Overall, both NP formulations of N3P represent promising approaches for treatment of TMZ-resistant DIPG and merit the next phase of preclinical evaluation.

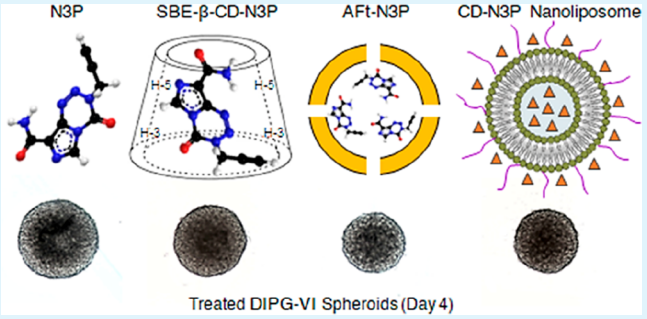

KEYWORDS: *diffuse intrinsic pontine glioma, DIPG, Temozolomide, TMZ, N(3)-propargyl, N3P, drug delivery, apoferritin, AFt, nanoliposome*

1. INTRODUCTION

Diffuse midline glioma/diffuse intrinsic pontine glioma (DIPG), which represent ∼75% of brainstem gliomas in children, are malignant infiltrative tumors of the ventral pons for which no effective therapeutic option currently exists.[1] Due to their diffuse and critical anatomic location, DIPG is inoperable and is associated with poor prognosis and median survival (<1 year). Unlike adult high-grade gliomas (aHGGs), the use of the frontline DNA methylating prodrug temozolomide (TMZ) in pediatric DIPG failed to give a clinical advantage over the standard short-time benefit of radiotherapy.[2] TMZ tumor resistance has been linked to the expression of the DNA repair enzyme O^6-methylguanine-DNA-methyl-transferase (MGMT)[3] and deficiency in DNA mismatch repair (MMR) proteins resulting in tolerance to O^6-methylguanine-thymine DNA mismatch.[4]

The novel N(3)-propargyl derivative of TMZ (N3P), where N(3)-methyl was replaced with a propargyl moiety, was demonstrated to evade recognition and removal by MGMT

Received: March 8, 2021
Accepted: June 7, 2021

Scheme 1. (A) Chemical structures of TMZ, N3P, and SBE-β-CD; (B) Illustration of SBE-β-CD-TMZ/N3P inclusion complexes; (C) Illustration of the encapsulation of TMZ/N3P into AFt by the nanoreactor route; (D) Illustration of the encapsulation of SBE-β-CD-TMZ/N3P complexes into nanoliposomes

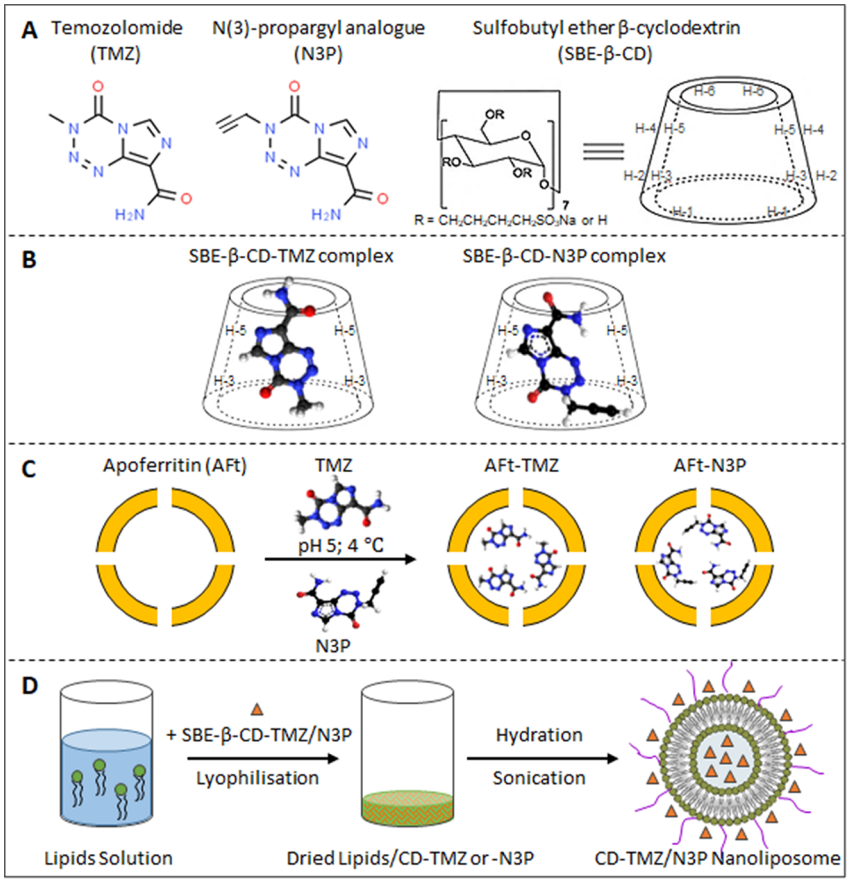

and exert activity independent of MMR status.[5,6] Despite desirable potency in MGMT$^+$ tumor cells, N3P demonstrated suboptimal drug metabolism (instability) and inferior pharmacokinetic properties ($t_{1/2}$ = 49 min *vs* 92 min for TMZ) at physiological pH.[7] The hindering blood−brain barrier (BBB) and presence of drug efflux transporters such as permeability-glycoprotein 1 (P-gp 1) or breast cancer resistance protein (BCRP) also limit the therapeutic potential of these drugs via systemic routes of administration.[8−10] Indeed, it has been estimated that less than 1% of the fraction of intravascular drug reaches the tumor.[11] Furthermore, systemic toxicities such as dose-related TMZ myelosuppression and lymphopaenia negatively impact the therapeutic window of the administered drug.[12,13]

Convection-enhanced delivery (CED) is a novel neurosurgical method of direct brain parenchymal drug delivery that bypasses the BBB utilizing localized bulk flow of drugs infused through stereotactically inserted intracranial microcatheters.[14] CED leads to significantly greater in situ drug concentrations than those achieved via systemic blood administration.[15] The pressure-driven fluid convection enhances drug delivery throughout the tumor mass. This strategy achieves much larger volumes of distribution compared to passive diffusion-controlled deliveries such as implantable polymeric wafers (Gliadel) or intratumoral injection.[16] In addition, drug compartmentalization within the brain ultimately minimizes systemic toxicities.

Despite these benefits, many drugs are unsuitable for CED as they are poorly soluble or show high tissue affinity and, as a result, encounter limited distribution and tumor penetration or are subject to high rates of elimination by transport into cerebrospinal fluid and blood.[17] Drug delivering nanoparticles (NPs) have however greatly enhanced CED dispersion and retention, and their application offers a promising alternative to repeat dosing of chemotherapeutics.[18] These have been chemically adjusted to cross the BBB and conjugated to moieties that target overexpressed receptors in the brain or respond to internal/external stimuli.[19] Recently, we have shown substantial survival benefit, tissue retention, and reduced neuronal toxicity of CED-administered nanomicellar panobinostat and carboplatin-loaded poly(lactic-*co*-glycolic acid) (PLGA) NPs over free drugs in rat glioma models.[20,21] However, PLGA NPs showed a burst release and low drug loading efficiency profile combined with reproducibility issues, while the pluronic nanomicelles underwent rapid clearance *in vivo*. Accordingly, in this study we investigated novel nanoparticulate transporters of TMZ and N3P to overcome their challenging low aqueous solubility and stability in physiologic milieu, thereby optimizing their suitability for CED.

We developed three nanodelivery systems of TMZ/N3P including an apoferritin (AFt) nanocage, a sulfobutyl ether β-cyclodextrin (SBE-β-CD) nanocomplex, and SBE-β-CD in nanoliposomes to improve their physicochemical and pharmacological properties *in vivo* (Scheme 1). The naturally

https://doi.org/10.1021/acsami.1c04164
ACS Appl. Mater. Interfaces XXXX, XXX, XXX−XXX

derived AFt (~444 kDa) is a biocompatible protein nanocage (~12 nm) with an internal cavity (~8 nm) suitable for loading of a variety of small molecules through its hydrophilic and hydrophobic channels (~3−4 Å).[22] AFt takes advantage of specific binding to the overexpressed transferrin receptor 1 (TfR1) on human cancer cells[22] and displays a pH-dependent drug release at a lower pH of the tumor microenvironment where its channels become swollen.[23,24] The FDA-approved SBE-β-CD (Captisol) is a hydrophilic β-cyclodextrin oligosaccharide derivative containing a hydrophobic internal cavity (~0.6 nm). It is specifically useful for complexation of insoluble compounds, replacing the use of organic solvents and surfactants in their formulations.[25] Recently, drug-in-cyclodextrin inclusion complexes have been encapsulated into nanoliposomes, consisting of one or more lipid bilayers enclosing an internal aqueous cavity, to provide a controlled drug release system.[26] This novel concept benefits accommodation of insoluble drugs in the aqueous core of nanoliposomes via cyclodextrins, thereby enhancing the incorporation rate and tempering drug−lipid membrane interaction and leakage out of liposomes.[27,28]

We hypothesized that localized intratumoral delivery of TMZ- and N3P-loaded NPs via CED would bypass the BBB and provide wider distribution and longer residence time within the tumor interstitial space. This approach also takes advantage of the TMZ/N3P rapid activation profile (high tumor toxicity) and rapid turnover (low systemic toxicity) after release. Since the physicochemical characteristics of each nanocarrier are distinct, we compared TMZ/N3P NPs (<100 nm) with regards to their therapeutic activity *in vitro* in DIPG models and their *in vivo* distribution following CED infusion.

2. MATERIALS AND METHODS

The full list of chemicals and reagents is provided in the Supporting Information.

All animal work was performed in accordance with the UK Animal Scientific Procedures Act 1986 and was covered by both project and personal licenses that were issued by the Home Office. Animal licenses were reviewed and approved by the University of Bristol and Nottingham Ethics Committee (project license PA95E951). All efforts were made to minimize animal use.

NPs Preparation. *TMZ/N3P-SBE-β-CD Nanocomplexes.* The solid TMZ and N3P-SBE-β-CD inclusion complexes (CD-TMZ or CD-N3P) were prepared in a stoichiometric molar ratio of 1:1.5 using a solution-stirring method followed by lyophilization.[29] Typically, the dry powders of drugs and SBE-β-CD were mixed and dissolved in acetate buffer (0.1 M, pH: 5) while stirring for 24 h at room temperature (RT). After reaching equilibrium, the mixture was freeze dried and stored at −20 °C. The complexes were then redissolved in deionized (DI) water with a brief bath sonication (~1 min) and sterilized through a 0.22 μm filter.

TMZ/N3P-Loaded AFt Nanocages (AFt-TMZ or AFt-N3P). AFt−drug formulations were prepared as described before[30] with some modifications. Briefly, after ferritin demineralization, drug solutions in dimethyl sulfoxide (DMSO) were diffused into an AFt nanocage (~1500 drug/AFt molar ratio) in 0.1 M sodium acetate buffer (pH 5) at 4 °C overnight. The formulations were then ultrafiltered using an Amicon Ultra 4 mL centrifugal filter, 30 kDa molecular weight cutoff (MWCO) (Merck Millipore, USA), washed with fresh buffer, ultrafiltered again, and sterilized through a 0.22 μm filter.

CD-TMZ or CD-N3P-Loaded Nanoliposomes. CD-TMZ- or CD-N3P-loaded nanoliposomes (Lip-TMZ or Lip-N3P) were prepared by a freeze-drying method as reported previously.[31] Initially, a homogeneous solution of lipids (cholestrol/1,2-dipalmitoyl-*sn*-glycero-3-phosphocholine/1,2-distearoyl-*sn*-glycero-3-phosphoethanolamine-*N*-[methoxy(polyethylene glycol)-2000] (ammonium salt), 37.4:60.6:2 molar ratio), plus mannitol (2.5% w/v) was prepared in 1:1 v/v tertiary butanol/acetate buffer (0.1 M, pH: 5) containing CD-TMZ or CD-N3P complexes. The mixture was then freeze dried by a Scanvac CoolSafe freeze dryer (LaboGene, Denmark) overnight, and the lyophilized powder was reconstituted in DI water. The resulting suspension was then sequentially subjected to a brief bath sonication (~2 min) to form a homogeneous dispersion of nanoliposomes.

Fluorescently Labeled NPs. A fluorescein isothiocyanate (FITC)-labeled solution of SBE-β-CD was prepared as described previously with some modifications.[32] Briefly, 3.8 mg of FITC (Thermo Fisher Scientific, USA) in 200 μL of DMSO was introduced dropwise into 2 mL of 0.75% SBE-β-CD in sodium hydroxide (0.1 M, pH 10.5). The mixture was magnetically stirred at RT for 24 h in the dark. The resultant FITC-labeled SBE-β-CD was dialyzed against DI water (Float-A-Lyzer G2, 0.5−1 kDa MWCO) in the dark to remove unreacted FITC molecules. AFt was tagged with a cyanine fluorescent dye (Cy5.5) through an *N*-hydroxysuccinimide (NHS)-amino coupling reaction as previously reported.[33] Briefly, the Cy5.5-NHS (Thermo Fisher Scientific, USA) was dissolved in dry DMSO and added to AFt solution at a dye to AFt molar ratio of 20:1 in 1× phosphate buffered saline (PBS, pH 8). The mixture was gently stirred overnight at 4 °C in the dark and then dialyzed (Float-A-Lyzer G2, 8−10 kDa MWCO) against 1× PBS (pH 7.4) to remove free dyes. For the preparation of fluorescently labeled nanoliposomes, the lipophilic membrane stain DiD (AAT Bioquest Inc., USA) was added to the lipid phase (0.5% molar ratio) during fabrication, and the final product was dialyzed (Float-A-Lyzer G2, 8−10 kDa MWCO) against 1× PBS (pH 7.4) to remove free dyes.

Zirconium-89 (^{89}Zr)-Radiolabeled NPs. ^{89}Zr was produced via proton bombardment of an yttrium target as described.[34] Protein concentration measurements were made on a DS-11-spectrophotometer (DeNovix Inc., USA), and radioactivity was determined using a CRC-25R dose calibrator (Capintec Inc., USA). Instant thin-layer chromatography (iTLC) was performed on glass microfiber chromatography papers (Agilent Technologies, USA), and strips were analyzed on the scan-RAM radio-TLC scanner (Lablogic System Ltd., UK). Radio-HPLC analytical evaluations were performed on an Agilent 1200 Series system with a Superdex 200 Increase small-scale size exclusion chromatography (SEC) column (GE Healthcare Life Sciences, USA) coupled with a Flow-RAM radio-HPLC detector (Lablogic System Ltd., UK).

AFt Modification with p-Isothiocyanatobenzyl-desferrioxamine (p-SCN-Bn-DFO). To a solution of AFt (5.8 mg/mL) in sodium bicarbonate (0.1 M, pH 9), a 10-fold molar excess of *p*-SCN-Bn-DFO (5 mM in anhydrous DMSO) was added. The volume of the *p*-SCN-Bn-DFO solution transferred to the protein solution was kept below 2% (v/v) to avoid precipitation. The reaction mixture was incubated at 37 °C for 1 h with gentle shaking (450 rpm), and the excess *p*-SCN-Bn-DFO was removed by Sephadex G-25 PD-10 desalting SEC columns (GE Healthcare Life Sciences, USA), eluting with 1.5 mL fractions of 1× PBS (pH 7.4). After combining the fractions, which corresponded to the DFO-modified AFt, the sample was concentrated using an Amicon Ultra-0.5 mL centrifugal filter (30 kDa MWCO, Merck Millipore, USA).

^{89}Zr Radiolabeling of DFO-AFt Conjugate. ^{89}Zr in 1 M oxalic acid was adjusted to pH 7−8 by the addition of 1 M sodium carbonate. The pH-adjusted solution was added to a 2.3 mg/mL solution of DFO-AFt to achieve a ratio of 0.033 MBq to 1 μg of AFt. The reaction mixture was incubated at RT for 1 h, and the radiolabeling efficiency was determined by iTLC using an eluent of 50 mM diethylenetriamine pentaacetate (DTPA, pH 7) and radio-HPLC. The crude reaction mixture was purified by a Sephadex G-25 PD-10 desalting column, and the radiochemical purity of the ^{89}Zr-DFO-AFt fraction was determined by iTLC and radio-HPLC.

Preparation of Nanoliposome-Encapsulated ^{89}Zr-DFO. A 22.5 mg total amount of freeze-dried lipids was reacted with 300 MBq of ^{89}Zr-DFO in 3 mL of 1× PBS (pH 7.4). The mixture was vortexed and sequentially subjected to a brief bath sonication (~2 min) to form a homogeneous dispersion of nanoliposomes. The reaction mixture was then incubated at 8 °C overnight with gentle shaking (450 rpm),

https://doi.org/10.1021/acsami.1c04164
ACS Appl. Mater. Interfaces XXXX, XXX, XXX−XXX

and the free ^{89}Zr-DFO was removed by a Sephadex G-25 PD-10 desalting column. The purified ^{89}Zr-DFO-nanoliposomes were then concentrated on Vivaspin 6 centrifugal concentrators (100 kDa MWCO, Sartorius, Germany), and the radiochemical purity was determined by radio-HPLC.

Nanoconstructs Characterization. *Analysis of Complex Formation.* One-dimensional proton nuclear magnetic resonance (^{1}H NMR) spectra of the free TMZ/N3P, SBE-β-CD, and CD-TMZ/N3P complexes were recorded on a Bruker NMR spectrometer (Avance III 400 MHz, Switzerland) in D_2O at 25 °C. Chemical shifts (δ) were reported in parts per million from that of DSS (4,4-dimethyl-4-silapentane-1-sulfonic acid) as an internal reference.

Aqueous Solubility of TMZ/N3P vs CD-TMZ/N3P Complexes. The water solubility of free TMZ/N3P and CD-TMZ/N3P inclusion complexes was quantified by suspending 5 mg of an equivalent amount of free TMZ/N3P or CD-TMZ/N3P complexes in 1 mL of acetate buffer (0.1 M, pH: 5) while stirring at 25 °C for 24 h. The suspensions were then filtered through 0.2 μm Minisart-SRP 15 syringe filters (Sartorius, Germany) and analyzed by UV−Vis spectroscopy (λ = 322 nm, N3P; λ = 330 nm, TMZ).

Analysis of NPs Size, Surface Charge, and Morphology. The hydrodynamic size and polydispersity index (PDI) of the NPs were measured at 25 °C (scattering angle of 173° to the incident beam, 100× dilution in DI water) on a Zetasizer Nano-ZS dynamic light-scattering instrument (Malvern Instruments, UK). The surface charge (ζ-potential) of the NPs was determined in DI water (25 °C) with a Zetasizer Nano-ZS according to their electrophoretic mobility within the Smoluchowsky approximation. The morphology of NPs was observed under a Tecnai G2 12 Biotwin transmission electron microscope (TEM, FEI, USA), where a small amount of diluted samples in DI water was applied onto the carbon-coated copper TEM grids and stained with 2% uranyl acetate prior to imaging.

Encapsulation Efficiency (EE). Drug EE was determined from absorbance measurements using a Fluostar OPTIMA plate reader (BMG Labtech, Germany). Purified NPs were first mixed with acetonitrile (1:10 v/v) for drug extraction, liposome destabilization, and SBE-β-CD/protein precipitation. The supernatants-containing drugs were then purified by centrifugation at 19 000g for 5 min and analyzed by UV−Vis spectroscopy.

NPs Drug Release Profile. The *in vitro* drug release kinetics of the developed nanomedicines was analyzed by a diffusion method. Drug-loaded NPs and free drugs (1 mg/mL; 5 mL) were loaded into Float-A-Lyzer G2 (8−10 kDa MWCO) devices and placed into a tube containing 45 mL of acetate buffer (0.1 M, pH 5.5) or PBS (1×, pH 7.4) under gentle shaking at 37 °C. For each designated time point, 0.5 mL of the sample was collected and replaced with the same amount of fresh buffer. All of the collected samples were further diluted appropriately and analyzed by their absorbance as described in previous sections.

***In Vitro* Cellular Experiments.** *Cell Lines.* The DIPG cell lines (DIPG-IV and DIPG-VI, MGMT$^+$; and DIPG-XIX, MGMT$^-$) were originally isolated from DIPG patients at Stanford University conducted with Institutional Review Board approval. These cells were obtained from Dr. Michelle Monje (Stanford University) through a Material Transfer Agreement (MTA). MGMT$^-$ patient-derived SF7761 cell line was originally isolated from DIPG tumor tissue acquired by the University of California San Francisco (UCSF) Tissue Bank through an approved Committee on Human Research protocol. For the present study, this cell line was obtained from Professor Nalin Gupta (UCSF) under MTA. All four cell lines were received in 2015 and authenticated by short tandem repeat (STR) profiling (Public Health England, UK). Cells were cultured and used within 10 passages from thawing under conditions described in the Supporting Information and confirmed to be mycoplasma free (in-house testing).

NPs Cellular Uptake Profile. The intracellular localization of the NPs was visualized under a confocal laser scanning microscope (Zeiss LSM 410, Switzerland). The DIPG-IV (MGMT$^+$) and DIPG-XIX (MGMT$^-$) cells were seeded (5×10^4 cells/well, 1 mL culture medium) on 4-well Nunc Lab-Tek II Chamber Slide System (Thermo Fisher Scientific, USA) and cultured for 48 h (37 °C, 5% CO_2). Cells were then incubated with fluorescently labeled NPs for 1 or 4 h. Subsequently, the medium was removed, and cells were washed with PBS and fixed in 4% paraformaldehyde (PFA) for 20 min at RT. The cells were further rinsed with PBS, and the actin cytoskeleton was stained with either 1× Phalloidin-iFluor 555 Conjugate or Alexa Fluor 488 Phalloidin (1/20, Cell Signaling Technology, USA) in PBS for another 20 min in the dark. Cells were rinsed gently with PBS to remove excess phalloidin conjugates and were then covered with sufficient 300 nM 4′,6-diamidino-2-phenylindole (DAPI) stain solution (Thermo Fisher Scientific, USA) for 5 min in the dark to label the nucleus. Finally, the solution was removed, and the cells were rinsed gently with PBS and mounted in Dako fluorescent mounting medium (Dako, USA). Images were captured using the Zeiss LSM 410 confocal laser scanning microscope (20× Olympus objective) and processed with the LAS X imaging software.

Two-Dimensional (2D) Cell Proliferation Assay. The DIPG cell lines were seeded in 96-well plates (5000−10 000 cells/well) in 100 μL of cell culture medium and incubated at 37 °C in a humidified atmosphere with 5% CO_2. The cells were treated 48 h later with equivalent concentrations (0−400 μM) of free TMZ, N3P, or TMZ/N3P-loaded NPs (n = 4) and incubated for 72 h. Blank NPs were used as controls for corresponding concentrations. Cell viability was analyzed using PrestoBlue reagent (Thermo Fisher Scientific, USA) according to the manufacturer's protocol and quantified by a Fluostar OPTIMA plate reader (BMG Labtech, Germany; excitation 544 nm and emission 590 nm). Three independent experiments were repeated for each condition, and the number of viable cells was normalized to nontreated cells. The sensitivity to the administered therapies was assessed by the concentration required to inhibit 50% cell growth (IC_{50}) calculated from logarithmic dose−response curves via GraphPad Prism 7.0 software.

Three-Dimensional (3D) Tumor Spheroids for Anticancer Drug Screening. For spheroid generation, 200 μL/well of cell suspensions at optimized densities (2.5×10^3 cells/mL; DIPG-IV and DIPG-VI) or (3.75×10^3 cells/mL; DIPG-XIX and SF7761) were dispensed into 96-well, ultralow attachment (ULA) round-bottomed plates (Corning Inc., USA). Plates were incubated for 4 days at 37 °C in a humidified atmosphere with 5% CO_2. Day 4 tumor spheroids (~300 μm in diameter) were then treated with controls and TMZ or N3P formulations at 50, 100, or 400 μM concentrations in fresh medium, and their growth was compared between groups. Spheroids were imaged using an inverted microscope (Nikon Eclipse Ti, Japan), and the mean diameter [$d = (a \times b)^{1/2}$] of each spheroid was calculated by measuring two orthogonal diameters from each spheroid (a and b) using ImageJ software. The volume of each spheroid ($V_{spheroid}$) was then evaluated by the equation $V_{spheroid} = 4 \times \pi \times (d/2)^3/3$. Responses were reported by $V_{spheroid}$ measurements pretreatment (day 4) and daily afterward.

At the end of the experiment, control spheroids (DIPG-IV and DIPG-XIX) were collected, washed with PBS, embedded in molten HistoGel specimen processing gel (Thermo Fisher Scientific, USA), and transferred into Tissue-Tek Cryomold molds (Sakura Finetek UK Ltd., UK). Solidified blocks were fixed in 4% PFA for 2 h, tissue processed on a Leica Peloris (Leica Biosystems, Germany), and embedded in paraffin. Blocks were then sectioned in 5 μm thick slices (Leica Microsystems, Germany), mounted on slides, stained with hematoxylin and eosin (H&E), and imaged using an inverted microscope (Nikon Eclipse Ti, Japan).

Western Blotting. The levels of MGMT, key MMR proteins (MLH-1, MSH-2, and MSH-6), P-gp 1/BCRP drug efflux transporters, and TfR1 expression in DIPG cell lines were assessed by Western blotting. Cell pellets were lysed in NP-40 lysis buffer [150 mM sodium chloride (NaCl), 0.5% NP-40, 1 mM ethylenediaminetetraacetic acid (EDTA), 50 mM Tris pH 7.4] supplemented with cOmplete, Mini, EDTA-free Protease Inhibitor Cocktail (Sigma, USA) for 30 min on ice. Equal quantities of total protein lysates (20 μg, as determined via Bradford Assay[35]) were resolved on 8% or 12% w/v polyacrylamide gel, and proteins were transferred to an Amersham Hybond-P 0.45 PVDF membrane (GE Healthcare,

https://doi.org/10.1021/acsami.1c04164
ACS Appl. Mater. Interfaces XXXX, XXX, XXX−XXX

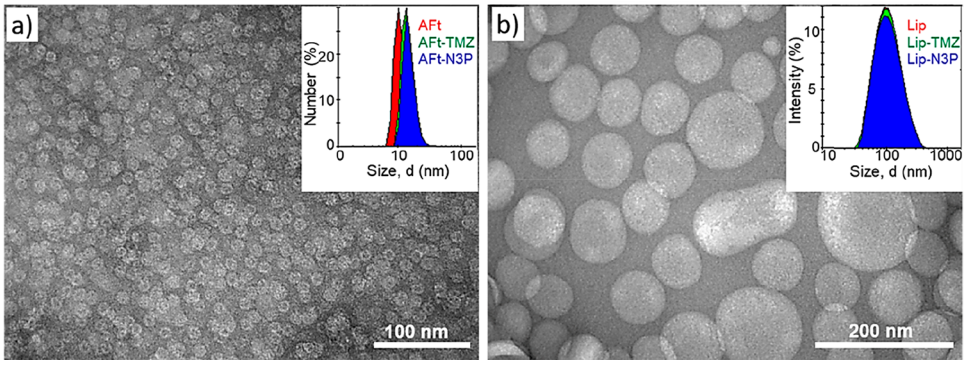

Figure 1. Representative TEM images of AFt-N3P (~14 nm) at 160k× magnification (a) and Lip-N3P (~77 nm) at 87k× magnification (b). Size distributions measured by DLS are shown in corresponding insets as number frequency curves of control AFt, AFt-TMZ, and AFt-N3P and intensity frequency curves of control Lip, Lip-TMZ, and Lip-N3P at 25 °C in DI water.

USA). The membrane was blocked with 5% w/v nonfat Marvel milk or 5% w/v bovine serum albumin in Tris-buffered saline (25 mM Tris pH 7.6, 0.15 M NaCl) containing 0.1% v/v Tween-20 (TBST) at RT for 1 h. It was then incubated with primary antibodies against TfR1, MSH-2, MSH-6, and GAPDH (1:1000, Cell Signaling Technology, USA), MGMT (1:50, Thermo Fisher Scientific, USA), P-gp 1 (1:1000, Abcam, UK), BCRP (1:100, Santa Cruz Biotechnology, Inc., USA), or MLH-1 (1:100, Sigma, USA) at 4 °C overnight. Subsequently, the membrane was washed with TBST and incubated for 1 h (RT) with horseradish peroxidase conjugated secondary antibodies. Finally, the specific proteins were identified using Pierce ECL Western Blotting Substrate (Thermo Scientific, USA) and scanned by a Fujifilm LAS-3000 Luminescent Image Analyzer (Fujifilm Life Sciences, USA).

***In Vivo* Experiments.** The CED procedure and biodistribution study were as follows. Juvenile male Wistar rats (Harlan, UK) weighing 250 ± 5 g were group housed in Techniplast 1500U cages with irradiated lignocel bedding and sawdust (International Product Supplies Ltd., UK). The study room was illuminated by a fluorescent light set to give a cycle of 12 h of light and 12 h of dark and was air conditioned. The ambient temperature was held between 17 and 22 °C. Animals were individually anaesthetised with 2% inhaled isoflurane (Baxter, USA) in oxygen in an anesthetic chamber and then placed in a stereotactic frame (David Kopf Instruments, USA). Anaesthesia was maintained with inhaled 2% isoflurane/oxygen, behind lead shielding. The scalp fur was clipped and skin cleaned using alcoholic chlorhexidine. A midline skin incision was made from glabella to occiput to expose bregma, and a small unilateral burr hole was drilled using a 2 mm drill through the skull. All CED procedures were performed using a 10 μL Hamilton syringe and rate-controlled microinfusion pump, as previously described.[21] The catheter tip was placed stereotactically into the striatum using coordinates derived from the Paxinos and Watson stereotactic rat brain atlas (3.0 mm lateral to bregma, 1 mm anterior from bregma, and 5 mm deep from the dura). ^{89}Zr or ^{89}Zr-labeled NPs (~1 MBq, 10 μL) were delivered at a rate of 1 μL/min over 10 min to the striatum. On completion of the infusion, the catheter was left in situ for 5 min and then withdrawn at a rate of 1 mm/min in order to minimize reflux. The wound was closed with 4/0 Vicryl (Bunzl, UK), and a dose of intramuscular analgesic (buprenorphine, 30 μg/kg, Centaur Services, UK) was administered. Dynamic positron emission tomography (PET) was then carried out on the animals at two time points (~20 min after infusion and 4 h later) using a nanoScan PET-CT (Mediso Ltd., Hungary), and data were processed with VivoQuant (Invicro, USA). Animals were euthanised by anesthetic overdose with an intraperitoneal injection of 1 mL pentobarbital (Euthatal; Merial Animal Health, UK). Radioactive uptake of areas of interest was measured and normalized to the initial injected dose.

Experimental values were normalized against negative and positive controls and presented as mean ± standard deviation (SD) from three independent experiments. Statistical analysis was performed using Graph Pad Prism 7.0 software. Significant differences between populations were determined using one-way analysis of variance and Tukey's multiple comparison post hoc analysis. Significance was defined as follows: (*) $P < 0.05$, (**) $P < 0.01$, (***) $P < 0.001$, or (****) $P < 0.0001$.

3. RESULTS AND DISCUSSION

Fabrication and Characterization of TMZ/N3P Nanoconstructs. Complexation of TMZ and N3P with the cyclic oligosaccharide SBE-β-CD was studied here as a route to overcome their poor aqueous solubility. Hydrophilic inclusion complexes were formed by aqueous solution stirring and freeze drying. UV−Vis spectroscopy elucidated that the resulting complexes increased the water solubility of TMZ or N3P by 2.33- or 3.34-fold as compared to the native drugs, respectively. The host−guest nonionic amphiphilic interactions between these drugs and SBE-β-CD in the liquid state were further investigated by analyzing their ^{1}H NMR complexation-induced hydrogen chemical shifts (Δδ). With respect to the free drugs, two prominent upfield chemical shifts were observed in the spectra of the nanocomplexes, which were assigned to the resonance of the shielded protons in the oxoimidazotetrazine ring (a) and carboxamide (b) region after complexation (Supplementary Figure S1, Supplementary Table S1). These changes together with slight downfield shifts of the SBE-β-CD interior cavity protons (H-3 and H-5) in the nanocomplexes elucidated that the aromatic ring of TMZ/N3P deeply inserts into the hydrophobic cavity of the SBE-β-CD. In contrast, the H-6 proton showed a slight upfield shift, which might be attributable to the increased electron density around the oxygen atoms at the primary hydroxyl narrow rim of the SBE-β-CD truncated cone structure via hydrogen bonding to the carboxamide region protons of the TMZ/N3P.

In order to achieve a higher drug payload per delivery system and sustained release activity, we then encapsulated CD-TMZ or CD-N3P water-soluble complexes within small nanoliposomes through our previously optimized method.[31] Likewise, the native drugs were also encapsulated via the nondisruptive nanoreactor route into an AFt nanocage in an acidic environment (pH 5) in order to avoid their degradation. The encapsulation of drugs had a negligible effect on the nanoliposomes' characteristics but slightly increased the hydrodynamic size of the AFt nanocage (14.6 *vs* 11.7 nm for AFt-N3P and control AFt, respectively), Supplementary Table S2. We detected approximately 712 TMZ and 631 N3P molecules per AFt nanocage after purification, disruption, and

https://doi.org/10.1021/acsami.1c04164
ACS Appl. Mater. Interfaces XXXX, XXX, XXX−XXX

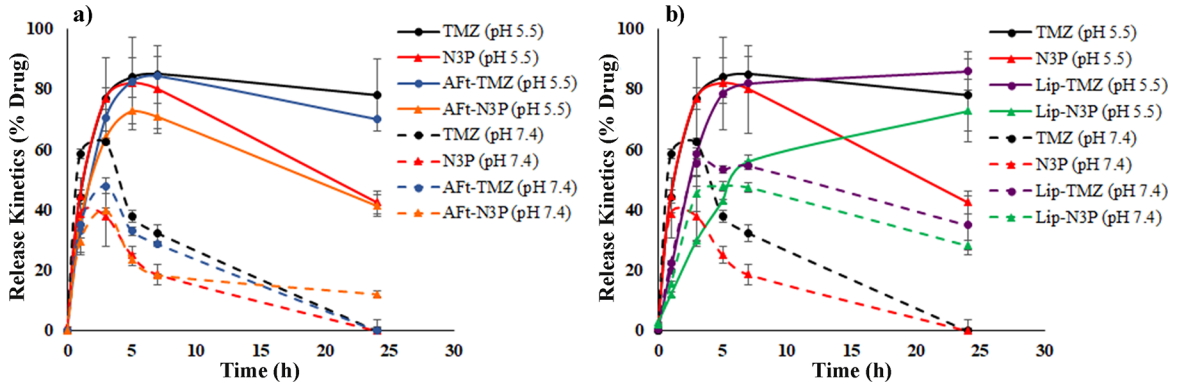

Figure 2. *In vitro* time course release profile of free TMZ/N3P and TMZ/N3P-loaded AFt (a) or Lip NPs (b) at 37 °C under two buffered conditions, pH 5.5 (0.1 M acetate buffer) and pH 7.4 (1× PBS). Formulations were filled in Float-A-Lyzer G2 (8−10 kDa MWCO) devices and placed into a tube containing 45 mL of release buffer under gentle shaking. At the specified time points, aliquots were removed and quantified by UV-Vis spectrophotometry. Data are presented as mean ± SD of samples from two independent experiments (n = 2).

extraction in acetonitrile, which were markedly higher than the rates reported in similar studies.[36,37] The quantification of active drugs within PD-10 column-purified nanoliposomes suggested an EE of ∼30%, which was slightly higher than a comparable study of liposomal TMZ prepared via a film hydration technique (EE of 23%).[38] According to this rate and assuming that ∼80 000 phospholipid molecules form 1 nanoliposome of ∼100 nm,[39] we obtained approximately 21000 drug molecules per nanoliposome. Therefore, a dramatically higher drug payload per particle was held in both NPs as compared to the nanocomplexes, which are also believed to achieve a longer clearance rate from the extracellular region relative to the free drugs. In addition, in order to take advantage of the rapid onset of action of the surface-adsorbed/nonentrapped CD-TMZ or CD-N3P complexes and the sustained and high intracellular release property of nanoliposomes, the nonpurified nanoliposomes were used in the cellular efficacy studies.

The NP formulations were fabricated reproducibly with desirable physicochemical properties for optimal CED drug delivery, as suggested earlier, including a NP size of <100 nm in diameter with a neutral or negative surface charge.[16] The TEM image of the NPs exhibited a uniform icosahedral (AFt-N3P) or smooth spherical (Lip-N3P) shape without aggregation (Figure 1a and 1b, respectively). The corresponding hydrodynamic diameter of the control NPs as illustrated by DLS measurements advocated their unimodal distribution with a number-weighted diameter of ca. 12 nm (AFt) and Z-average intensity-weighted diameter of 94 nm (nanoliposomes) (Figure 1a and 1b, respectively). The DLS diameter trends [14.6 ± 0.8 nm, AFt-N3P; 92.7 ± 1.2 nm, Lip-N3P] confirmed a slight increase *vs* those measured by TEM analysis [13.7 ± 0.8 nm, AFt-N3P; 77.1 ± 13.7 nm, Lip-N3P], suggesting the associated hydration shell around NPs when dispersed in DI water. In the case of nanoliposomes specifically with larger dimensions, a smaller number-weighted TEM size distribution was detected as compared to the intensity-weighted DLS data. According to the main classification of liposomes, which depend on the size and lamellarity, our nanoliposomes can be classified as unilamellar liposomes since multilamellar vesicles, which consist of several concentric bilayers, are larger in size (>500 nm).[40,41] Moreover, the cavitation events induced by sonication in the process of preparing our nanoliposomes would break up any larger multilamellar vesicles, turning them into small unilamellar vesicles.[42]

Zeta potential measurements detected a negative surface charge of ca. −14 mV for AFt NPs, attributed to its net negative charge over the isoelectric point (pH ∼ 4.4),[24] and ca. −32 mV for Lip NPs, likely due to the surface-adsorbed nonencapsulated SBE-β-CD molecules and shielding DSPE-mPEG-2000 on its surface (Supplementary Table S2). This anionic surface charge plus their small sizes (<100 nm) would facilitate the NPs stability (via electrostatic repulsion) and dispersibility in biological environments with minimal aggregation and reduced nonspecific binding to the extracellular matrix (ECM) during CED infusion. This important feature was discussed by MacKay et al., who determined that smaller nanoliposomes (40−80 nm) with a neutral or negative surface charge travel for longer distances than larger (200 nm) or positively charged liposomes that have high tissue affinity following CED to the rat brain.[43] The deformability feature of small nanoliposomes could potentially help them squeeze through brain extracellular space without losing their integrity.[43] Likewise, CED of NPs with sizes <100 nm in diameter was shown to improve their penetration through the brain parenchyma compared to larger particles.[44] Moreover, surface shielding with PEG polymers has been shown to substantially enhance diffusion and penetration of large polymeric NPs (>100 nm) within brain tissue by minimizing adhesive interactions with ECM.[45] Chen et al. demonstrated the inability of poly(ω-pentadecalactone-*co*-*p*-dioxanone) NPs to distribute within the brain (V_d/V_i <0.5), probably as a result of their large diameter (∼300 nm) and lack of PEG coating that results in significant aggregation at the site of infusion.[46] Overall, it has been proposed that nanocarriers beyond 100 nm or with high tissue affinity are unlikely to transit neocortical brain extracellular space.[16]

Both TMZ and N3P were stable in AFt and Lip NPs for at least 7 days at 4 °C with slight degradation thereafter (e.g., ∼10% loss of Lip-TMZ activity and ∼25% reduction of Lip-N3P activity after 3 weeks storage in the refrigerator). Analysis of the drug release kinetics from the NPs under physiologically simulating conditions [37 °C, pH 7.4 (blood−cerebrospinal fluid) and pH 5.5 (intracellular endosomes)], revealed a sustained release profile over 24 h (Figure 2). These results suggest that a longer exposure of tumor cells to drugs could be maintained after CED administration and tissue uptake,

https://doi.org/10.1021/acsami.1c04164
ACS Appl. Mater. Interfaces XXXX, XXX, XXX−XXX

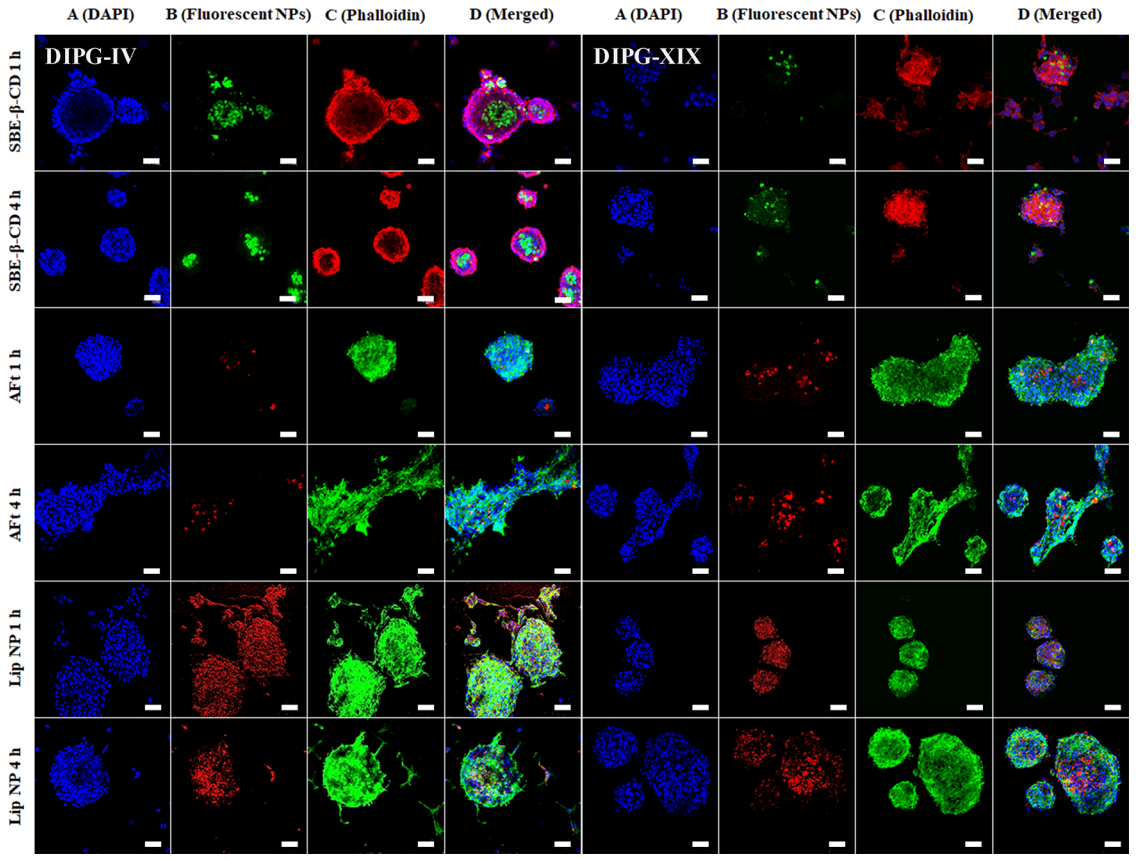

Figure 3. Confocal microscopic images of DIPG-IV and DIPG-XIX cells after 1 or 4 h incubation with FITC-SBE-β-CD, Cy5.5-AFt, and DiD-Lip NPs (B) at 37 °C. Actin cytoskeleton of cells (C) was stained with either Phalloidin-iFluor 555 conjugate (red) or Alexa Fluor 488 Phalloidin (green), and the nuclei (A) were stained with DAPI (blue). Column D shows the merged channels captured using the Zeiss LSM 410 confocal laser scanning microscope, 20× Olympus objective. Scale bar: 40 μm.

particularly with the larger Lip NPs. Previously, Park's laboratory showed a 22- and 66-fold increase in tissue half-life of nanoliposomal CPT-11 (irinotecan) over free CPT-11 following equivalent CED doses or at their highest tolerable dose in rat brains, respectively.[47] Similarly, CED administration of liposomes containing topotecan had a tissue clearance half-life of 1.5 days, in contrast to 0.1 days of free topotecan in healthy rat brains.[48]

The percentage release of detectable nondegraded N3P under susceptible condition (PBS 1×, pH 7.4) was significantly ($P < 0.05$) higher from NPs after 24 h (12.2%, AFt-N3P; 28.2%, Lip-N3P) relative to free N3P (0%), which corroborates its improved stability inside NPs. In contrast, at a relevant endosomal pH (0.1 M acetate buffer, pH 5.5), the amount of released N3P was quite similar between free or AFt-N3P at the end of the experiment. This is consistent with the expectation that AFt channels swell in a mild acidic environment,[49] leading to a fast drug diffusion which is comparable to that of the free N3P alone. The slower drug release profile of AFt-TMZ/N3P within the first 3 h of incubation at pH 7.4 *vs* pH 5.5 also reflects the slower diffusion through the narrower channels at neutral pH. Yet, Lip-N3P NPs still showed a significantly higher percentage release of N3P ($P < 0.05$), even at the stabilizing acidic pH compared to N3P alone after 24 h. This could be attributed to the slower release profile of the Lip-N3P with respect to AFt-N3P formulation, masking N3P slow degradation at pH 5.5 as compared to free TMZ with a higher stability profile.

Overall, the exchange of cargo between AFt's interior and exterior environments and through its hydrophilic and hydrophobic channels, each 3−4 Å in diameter,[50] seems to be faster than those encapsulated in the aqueous core of nanoliposomes with surrounded concentric lipid bilayers. AFt can immediately release part of its cargo upon dilution in a new medium, especially in a mild acidic environment where its channels swell.[49] Considering the short half-life of N3P ($t_{1/2}$ < 1 h) at physiologic pH, the released fraction is then subject to degradation over time while the encapsulated cargo inside nanoliposomes (~30%) is more stable.

***In Vitro* Cellular Evaluations.** Cellular uptake of fluorescently tagged NPs was then investigated in representative DIPG cell lines (DIPG-IV and -XIX) using confocal laser scanning microscopy. As shown in Figure 3, all of the nanoconstructs were visualized in the cytoplasm and perinuclear region of cells within 1 h of treatment. The SBE-β-CD signal also overlapped with the DAPI signal, indicating its accumulation in the nucleus, which could be attributed to the ability of cyclodextrins to disrupt cellular membranes.[51] Examining Z-stacks in the neurosphere clusters suggested the likelihood of NPs penetration deep into these structures. The visual uptake efficiency of AFt nanocages was detected to be higher in the DIPG-XIX ascompared to the DIPG-IV neurospheres, perhaps due to the higher expression of TfR-1 in these cells (Figure 4). However, the uptake profile of nanoliposomes was quite similar among the cell lines tested, and there was no noticeable change in the NPs uptake kinetics

https://doi.org/10.1021/acsami.1c04164
ACS Appl. Mater. Interfaces XXXX, XXX, XXX−XXX

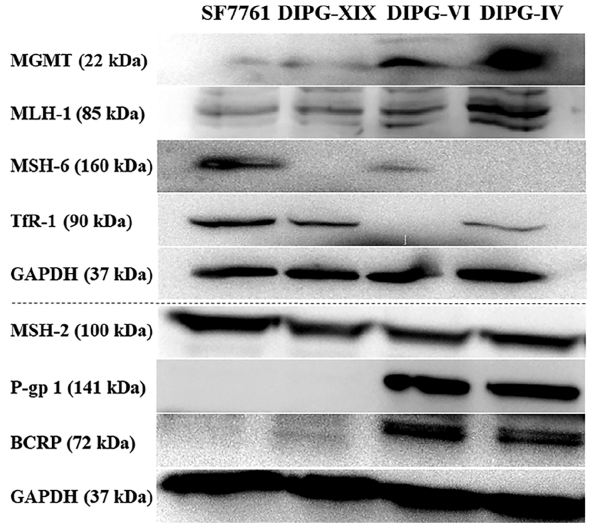

Figure 4. Western blot analysis of the intracellular DNA repair enzyme MGMT (responsible for TMZ resistance), MMR proteins (MLH-1, MSH-2, and MSH-6, required for TMZ activity), membrane-bound TfR1 (associated with AFt uptake), P-gp 1 and BCRP (drug efflux pumps), and loading control (GAPDH) in different DIPG cell lines.

after a longer 4 h incubation time. Previous investigation of endocytic pathways by live cell imaging of PEGylated anionic liposomes (~120 nm) in glioblastoma U87MG cells showed their time-dependent uptake via macropinocytosis, while in NIH/3T3 fibroblast cells, uptake was via clathrin-mediated endocytosis.[52]

Next, we investigated the 2D cytotoxicity of TMZ/N3P alone or when loaded into NPs by Presto Blue cell viability assay and characterized the sensitivity of DIPG cell lines toward test agents by analyzing their IC_{50} values, Table 1. For each condition, control NPs were tested and their biocompatibility was monitored. In general, the vehicle-associated toxicity was negligible with only minimal inhibition of cell proliferation occasionally observed at very high concentrations of control SBE-β-CD (IC_{50} > 2.1 mM, DIPG-IV) or control AFt (IC_{50} > 4.2 mM, DIPG-VI). Our results suggested the feasibility to preserve or enhance the cytotoxicity of TMZ and N3P against TMZ-resistant cell lines when encapsulated in the AFt or Lip NPs (Table 1). We also observed an identical concentration-dependent cytotoxicity profile between TMZ/N3P dissolved in DMSO and DMSO-free CD-TMZ or CD-N3P nanocomplexes, confirming that complexation does not compromise their activity. This is in contrast to another study by Yang et al.,[53] who reported the slight activity decline of anticancer alkaloid camptothecin after the grafting of β-CD in HCT-116 human colon cancer cells (relative cellular viability of 22% vs 35%, respectively). Therefore, use of SBE-β-CD to solubilize TMZ/N3P without the need for a toxic cosolvent like DMSO is a functional approach to preserve their activity but eliminate the cosolvent-related unfavorable cell death, particularly at higher concentrations tested *in vitro*.

As expected, TMZ was active in $MGMT^-$ SF7761 cells with functional MMR proteins (IC_{50} value of 49.17 μM) but impotent in MGMT-proficient and P-gp 1/BCRP drug efflux pumps expressing (DIPG-IV and -VI) or MSH-6-deficient DIPG-XIX cells (Table 1, Figure 4). However, consistent with data published previously on glioblastoma multiforme (GBM) cell lines,[5] N3P exerted its superior activity in TMZ-resistant

Table 1. IC_{50} of free TMZ/N3P, CD-TMZ/N3Pcomplexes, and TMZ/N3P-loaded AFt or Lip NPs against different DIPG cell lines (n = 3)

Cell Lines		IC_{50} ± SD (μM)											
										Controls			
		TMZ	CD-TMZ	AFt-TMZ	Lip-TMZ	N3P	CD-N3P	AFt-N3P	Lip-N3P	CD	AFt	Lip
$MGMT^+$	DIPG-IV	192.6 ± 1.83	198.5 ± 1.95	118.2 ± 1.86	134.1 ± 1.85	32.8 ± 1.92	22.8 ± 2.01	28.4 ± 1.88	14.6 ± 1.92	2161 ± 4.41	–	–
	DIPG-VI	7123 ± 4.57	6546 ± 4.12	442.9 ± 2.18	1541 ± 2.52	111.9 ± 1.84	114.6 ± 1.81	101.8 ± 1.85	140.4 ± 1.91	–	4294 ± 11.20	–
$MGMT^-$	DIPG-XIX	245.3 ± 1.87	229.2 ± 1.93	325.8 ± 2.10	402 ± 1.97	204.6 ± 2.01	219.3 ± 2.15	231.5 ± 2.01	247.4 ± 2.01	–	21 644 ± 2745	–
	SF7761	49.2 ± 1.92	48.5 ± 1.92	68.1 ± 1.98	73.5 ± 1.98	48.5 ± 1.89	53.6 ± 1.88	64 ± 1.84	64.5 ± 1.87	–	–	–

https://doi.org/10.1021/acsami.1c04164
ACS Appl. Mater. Interfaces XXXX, XXX, XXX−XXX

DIPG-IV and DIPG-VI cells independent of MGMT, drug efflux pumps, or MMR deficiency as summarized in Table 1. In particular, DIPG-VI cells were more insensitive to the effect of TMZ with an IC_{50} value > 7.1 mM. It is presumed that the lower expression of MLH-1 in these cells may have contributed to the substantially stronger TMZ resistance as compared to DIPG-IV cells (Figure 4, Table 1). Importantly, both AFt-TMZ and Lip-TMZ NPs displayed enhanced activity over naked TMZ in $MGMT^+$ cell lines as shown in Figure 5 with

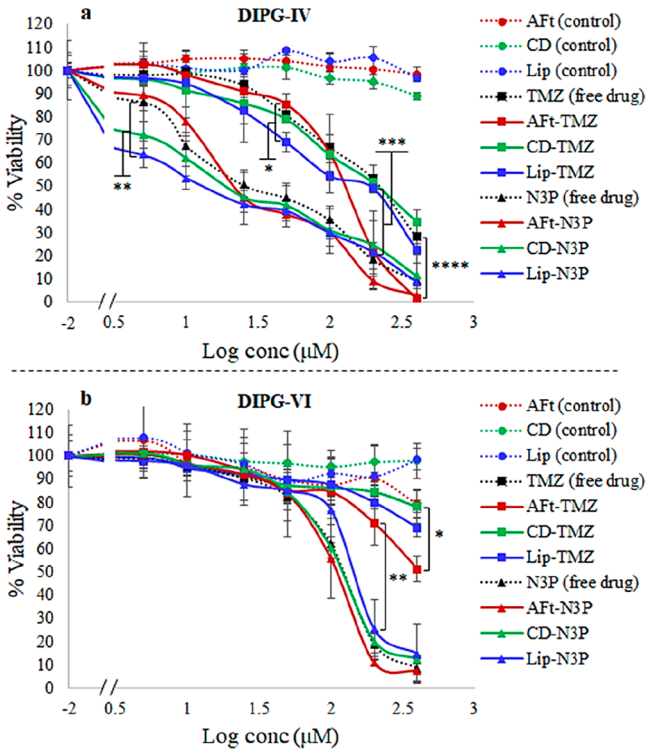

Figure 5. Cytotoxic effects of TMZ/N3P, CD-TMZ/N3P complexes, or TMZ/N3P-loaded AFt or Lip NPs in $MGMT^+$ DIPG-IV (a) and DIPG-VI (b) cell lines. Cells were treated with equivalent concentrations (0–400 μM) of drugs or control NPs in culture medium for 72 h at 37 °C. Data are presented as mean ± SD of samples from three independent experiments.

statistical significance indicators. Likewise, in a previous study we showed enhanced activity of AFt-TMZ in $MGMT^+$ GBM and MMR-deficient HCT116 colorectal carcinoma cells.[30] This was postulated as a consequence of enhanced TMZ delivery by AFt, overwhelming suicide repair protein MGMT as evidenced by enhanced O^6-methylguanine adducts, highly perturbed cell cycle profile, and increased DNA double-strand breaks (γH2AX foci).[30] The glioma drug-resistance attenuation was also reported through TMZ encapsulation into other nanostructures including chitosan, cucurbit[7]uril, lactoferrin, liposome-biomolecular corona complexes, and a tetrahedral framework DNA NP.[54−58] The sustained release kinetics (maintaining sufficient concentration) and physiologic stabilization or different mode of cellular uptake bypassing drug-efflux proteins was suggested for this TMZ-sensitization behavior via these NPs. On the other hand, free TMZ was functional in TMZ-responsive SF7761 cells and there was no advantage of using TMZ-loaded NPs in this cell line. Interestingly, at lower concentrations (5–25 μM), TMZ more efficiently inhibited the growth of these cells than N3P, an effect which was reversed at higher concentrations (>50 μM), Supplementary Figure S2. This is probably due to the superior stability profile of TMZ at physiologic pH, which grants its higher potency at very low concentrations as compared to N3P.

Dosing with AFt-N3P NPs potentiated the activity of N3P on both DIPG-IV and -VI cell lines (Table 1); however, this effect was not statistically significant. On the other hand, Lip-N3P NPs induced a significant decrease in DIPG-IV cell survival ($P < 0.01$, 10 μM) compared to free N3P. Remarkably, DIPG-XIX cells showed a differential reduced response toward AFt-N3P and Lip-N3P NPs. Since these cells grow as neurosphere 3D clusters in culture, this might represent a penetration barrier to the NPs, which was more apparent for larger Lip-N3P NPs > AFt-N3P NPs > CD-N3P > free N3P (Table 1, Supplementary Figure S2). Similar to TMZ-NPs, SF7761 cells were equisensitive to N3P-NPs as compared to free N3P.

We then developed multilayer 3D spheroids to mimic the *in vivo* tumor biology using optimized cell densities and analyzed their response toward selected doses of therapeutics (50 and 100 μM of N3P; 100 and 400 μM of TMZ) representing the 2D IC_{50} values. The safety of the control nanovehicles was also ensured at the equivalent 100 μM concentration for all cell lines, whereas at a higher concentration (400 μM) they showed variable restrictions for DIPG spheroids growth (Supplementary Figure S3). The spheroids where characterized with a rounded or oval morphology in phase-contrast images, and their H&E-stained sections revealed a more packed cellular organization in some (e.g., $MGMT^+$ DIPG-IV) as compared to a more loose architecture in others (e.g., $MGMT^-$ DIPG-XIX), Supplementary Figure S4. This differential morphology can have a substantial impact in terms of NPs' penetration and efficacy.

Consistent with the effect of other classical chemotherapy drugs such as paclitaxel, cisplatin, and docetaxel in 3D cancer models,[59−61] our compact DIPG-IV spheroid cultures generally displayed a more resistant proliferative response toward free N3P or N3P NPs as compared to the 2D model. This reduced potency was proposed to be a consequence of barriers such as diffusion gradients, increased expression of proteins involved in cell survival, or transporters associated with drug resistance. However, a longer incubation time could increase the free drug therapeutic efficacy as shown in Supplementary Figure S5. On the other hand, in DIPG-XIX spheroids with a more permeable structure, the N3P and N3P NPs showed an enhanced response over their 2D results (Supplementary Figure S5). It appears that penetration of N3P molecules deeply into the acidic spheroid cores may mitigate their premature degradation (because of relative acid stability) and thus compensate for the effect of transport barriers.

In agreement with our 2D results, for both $MGMT^+$ DIPG-IV and -VI cell lines, the free N3P or N3P-nanotherapeutic outcomes were significantly ($P < 0.01$) stronger on spheroids' growth inhibition as compared to free TMZ (Figure 6). In addition, both AFt-N3P and Lip-N3P NPs showed significantly ($P < 0.05$, 50 μM; $P < 0.01$, 100 μM) better response in contrast to free N3P on DIPG-VI spheroids (Figure 6 and Supplementary Figure S6). Four days incubation of DIPG-VI spheroids with 100 μM AFt-N3P, Lip-N3P, or CD-N3P caused 46%, 31.7%, and 28.5% reduction in their average volume growth rate relative to free N3P-treated percentage growth, respectively. The same pattern was seen in MMR-deficient

https://doi.org/10.1021/acsami.1c04164
ACS Appl. Mater. Interfaces XXXX, XXX, XXX−XXX

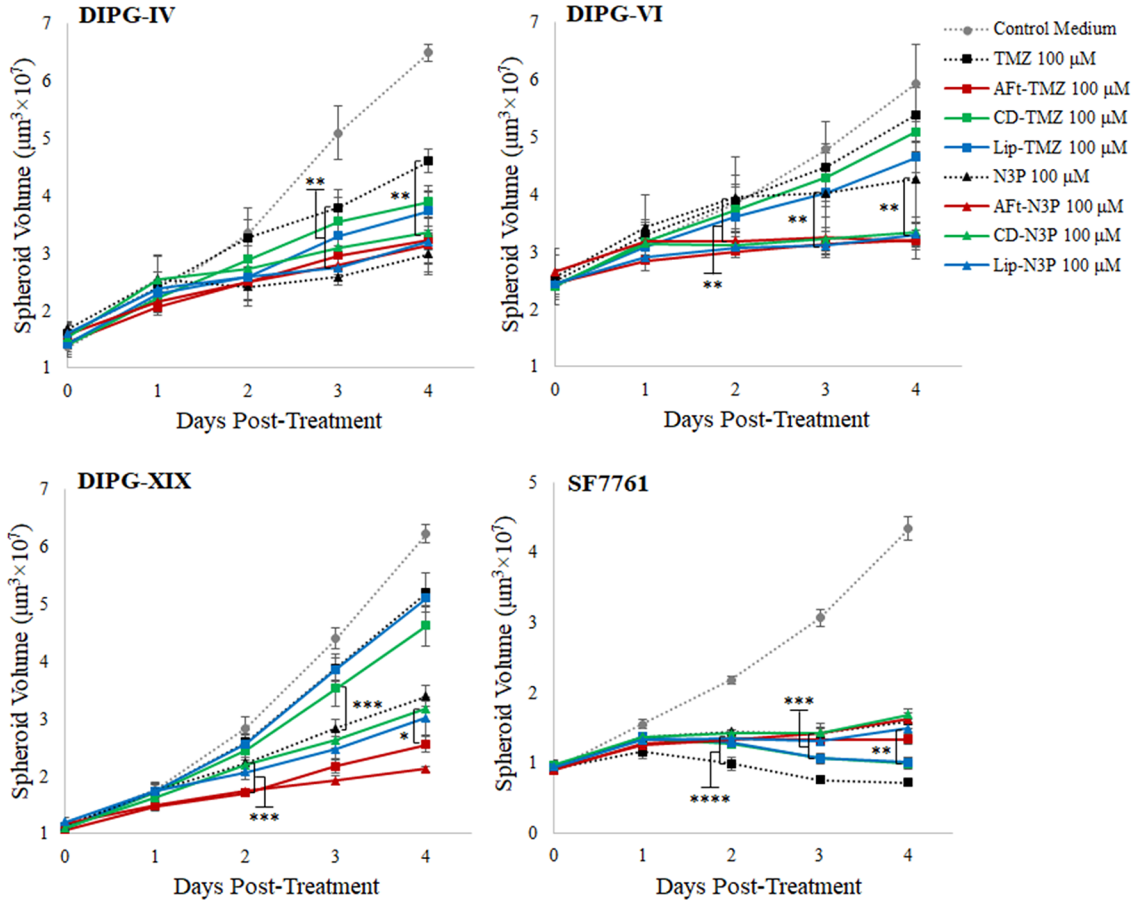

Figure 6. Growth inhibitory effects of TMZ/N3P, CD-TMZ/N3P complexes, or TMZ/N3P-loaded AFt or Lip NPs in various 3D DIPG spheroids. Spheroids were developed in ULA 96-well round-bottom plates and treated on day 4 (~300 μm) with 100 μM TMZ/N3P formulations or controls in fresh medium, and their growth was screened daily afterward. Values are means ± SD of five spheroids.

DIPG-XIX spheroids with a significant (P < 0.05, 50 μM) growth mitigation with both N3P-NPs and a substantially enhanced response (P < 0.0001, 100 μM) with AFt-N3P, corresponding to a 118.26% reduction in growth rate as compared to free N3P. The less potent inhibitory effect of Lip-N3P NPs in comparison to AFt-N3P NPs in this cell line is probably because of their larger size-related distribution/penetration barrier.

Figure 7 shows representative images of various DIPG spheroids before (day 0) and after exposure (day 4) to equivalent concentrations (100 μM) of free TMZ/N3P, TMZ/N3P-loaded NPs, or controls. Notably, the growth inhibitory effect of N3P-NPs was equivalent to that of the free drug alone in DIPG-IV spheroids, which could be attributed to their intrinsic penetration barriers as illustrated by the hindering compact outer layer cell organization (Supplementary Figure S4). It seems that in spheroid structures like DIPG-IV, the effect of nanoparticulate therapeutics is mainly restricted to their uptake profile by the outer layer cells, which needs further investigation. This variation in 3D spatial arrangement of spheroid structures and drug sensitivity (loose aggregates) or resistance (tight aggregates) was also reported earlier for breast cancer models.[62] Alterations in hypoxia, acidity, metabolic activity, ECM components, and their cellular interactions were also reported to alter drug responses in the spheroid cultures.[63]

Intriguingly, incubation with AFt-TMZ led to significant tumor growth repression (p < 0.001, 100 μM) as compared to free TMZ in MGMT$^+$ and MMR-deficient spheroid cultures (Figure 6). This effect was slightly mitigated at the higher 400 μM concentration where free TMZ was also equivalently effective on DIPG-XIX cultures (Supplementary Figure S7). The clear observations of spheroid shrinkage with apparent surface blebbing with 400 μM AFt-TMZ, which may signify enhanced apoptosis, are illustrated in Supplementary Figure S8. The enhanced response of TMZ when incorporated in AFt-NPs is in support of our 2D data and previous study on TMZ-resistant U373M GBM cells.[30] It was postulated that the different mode of cellular uptake (AFt-TfR1 internalization) and evasion of efflux transporters could finally enhance intracellular accumulation of TMZ and outpace MGMT levels. Indeed, TfR1 upregulation has been found in many types of tumors, which can lead to a high targeting efficiency of AFt in proliferating cancer cells with an increased iron demand.[22,64] Similar to our 2D observations, there was no advantage of using TMZ/N3P-NP formulations in TMZ-sensitive SF7761 spheroid cultures.

Radiosynthesis of NPs and *In Vivo* Brain Distribution and Retention Properties. New radiosynthesis methods were introduced to prepare AFt and Lip NPs containing PET-traceable ^{89}Zr ($t_{1/2}$ = 78.4 h) with high purity. The primary lysine-NH$_2$ groups of AFt were initially conjugated to the isothiocyanate group of the bifunctional p-SCN-Bn-DFO, a chelator for $^{89}Zr^{4+}$ radioisotope, via a stable thiourea linkage and purified using gel filtration (Scheme 2). The AFt-DFO conjugate was then radiolabeled with ^{89}Zr-oxalate with a radiochemical yield of 25.0 MBq/mg and a radiochemical

https://doi.org/10.1021/acsami.1c04164
ACS Appl. Mater. Interfaces XXXX, XXX, XXX−XXX

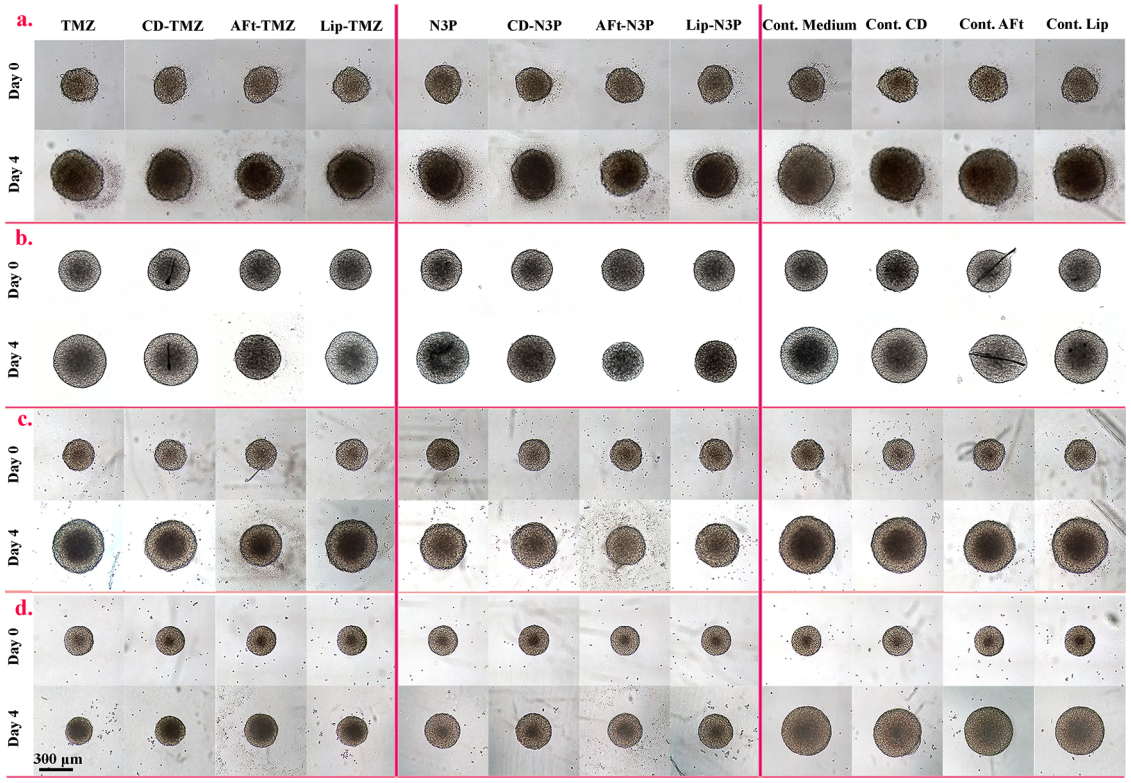

Figure 7. Representative images of DIPG-IV (a), DIPG-VI (b), DIPG-XIX (c), and SF7761 (d) spheroids obtained before (day 0) and 4 days post-treatment with 100 μM TMZ/N3P formulations or controls.

Scheme 2. Schematic Representation of Radiosynthesis Methods for Preparation of PET Traceable ^{89}Zr-AFt (a) and Lip NPs (b)

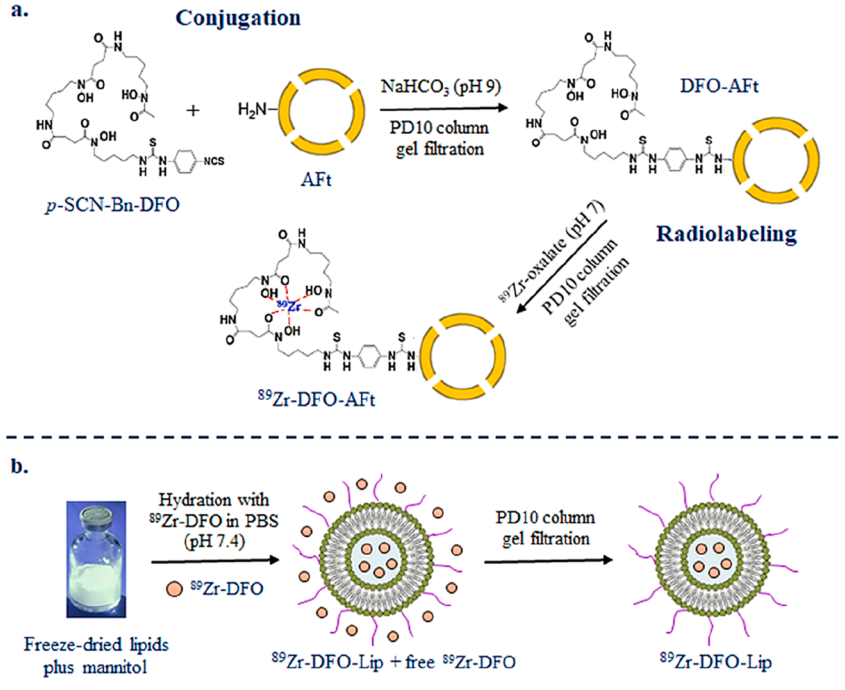

purity 100% as assessed by radio-TLC (Supplementary Figure S9). Representative SEC radio-HPLC chromatograms of ^{89}Zr-DFO and purified ^{89}Zr-DFO-AFt (specific activity of 24.2 MBq/mg) are shown in Supplementary Figure S10 with a shift in the peak retention time from 37.48 min for free ^{89}Zr-oxalate to 21.5 min for ^{89}Zr-DFO-AFt. In order to produce radiolabeled nanoliposomes, the ^{89}Zr-DFO complex was encapsulated into the aqueous cavity of nanoliposomes during hydration of the freeze-dried lipid film and the unencapsulated ^{89}Zr-DFO was removed by gel filtration (Scheme 2). The radiochemical purity of ^{89}Zr-DFO-liposome according to the analytical radio-HPLC (Supplementary Figure S10) was 100%

https://doi.org/10.1021/acsami.1c04164
ACS Appl. Mater. Interfaces XXXX, XXX, XXX−XXX

with a specific activity of 104 MBq/mL and with a shift in the peak retention time of ^{89}Zr-DFO from 37.43 to 15.1 min. Since ^{89}Zr-DFO physically encapsulates inside liposomes during their formation, the final radioactivity of the purified and concentrated samples were less than the purified ^{89}Zr-DFO-AFt samples (1 MBq compared to 5 MBq in 10 μL). There was no noticeable radiolabel leakage from the purified NPs when stored at 4 °C for at least 24 h as analyzed on radio-HPLC.

We then applied our CED method to effectively deliver the radiolabeled AFt NPs into the rat striatum and tracked their spatial volume of distribution (V_d) and retention using dynamic PET radiotracer signals postsurgery and subsequently 4 h postsurgery, Figure 8. Animals used within the study period showed no abnormal behavior after surgery. Retention of the ^{89}Zr-DFO-AFt NPs within the brain was observed with minor clearance and accumulation of the signal within the lymph system as demonstrated in the uptake in the manifold lymph nodes (Figure 8c and 8d). Figure 8d clearly demonstrates brain retention of ^{89}Zr-DFO-AFt NPs in the parenchyma and an accumulation in the lymph system. Quantitation data related to this in areas of interest is also shown in Figure 8e as percentage of radioactive uptake relative to the initial injected dose. The stability of the radiolabeled NPs is also observed at 4 h without free ^{89}Zr dispersed throughout the animal or uptake within bones.

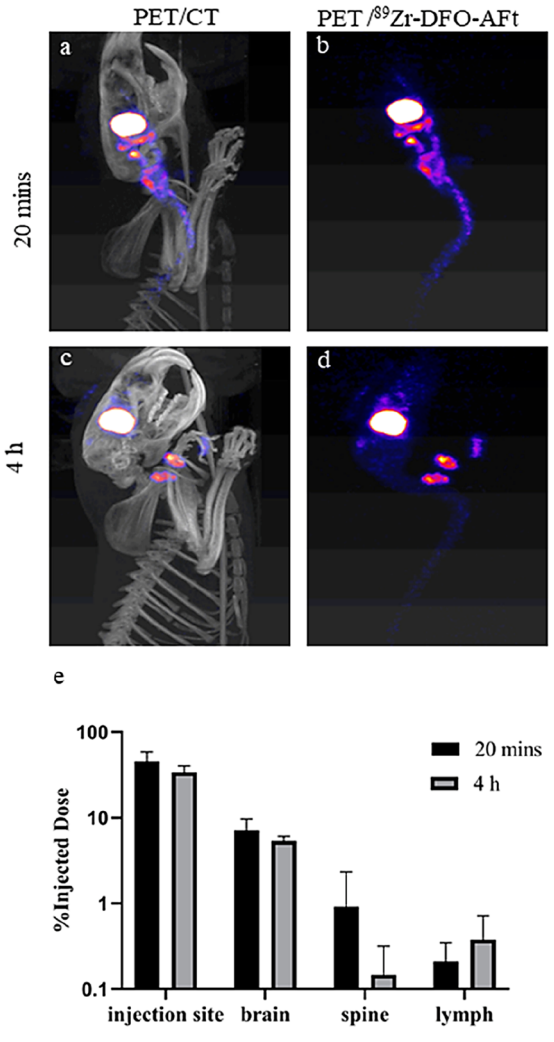

Figure 8. Representative *in vivo* PET/CT images of ^{89}Zr-DFO-AFt distribution in adult Wistar rats 20 min (a and b) and 4 h (c and d) after infusion. Following infusion, the injection bolus is retained within the brain parenchyma and drainage into the cerebrospinal fluid is observed (a–d). Accumulation of the signal over time in the lymph nodes (c–e) can be seen, and there was no associated bone uptake of ^{89}Zr-DFO-AFt NPs. (e) Data shows the percentage of radioactive uptake in areas of interest relative to the initial injected dose (mean ± SD; n = 3).

With respect to the infiltrative nature of DIPG, AFt NPs achieved a satisfactory distribution within the striatum following a single infusion. A substantially greater spatial V_d/volume of infusion (V_i) was achieved with our smaller sized ^{89}Zr-DFO-AFt NPs 4 h after CED (~14 nm, V_d/V_i ratio of ~5) in comparison to the larger sized Lip NPs (130 nm, V_d/V_i ratio of ~1).[38] Our 10 μL infusion results were quite similar to those achieved via 20 μL CED infusion of small polymeric PLGA NPs (71 nm, V_d/V_i ratio of ~5.5) delivered over 30 min to the striatum of Sprague–Dawley rats.[65] The restrictive behavior of NPs size on their distribution following CED should be complemented with their tissue retention and sustained release properties. For example, Chen et al. discussed the benefits of NP diameter in sustained distribution where larger but penetrable polymeric NPs (~106 nm) retained a substantially higher V_d as compared to the smallest NPs (~75 nm) 24 h after CED.[46] Therefore, optimizing the effect of NPs size on early penetration and sustained distribution within the brain following CED can potentially maximize their clinical efficacy.

Our investigation into the AFt NPs retention profile and spatial volume of the distribution when delivered via CED to the healthy brain striatum was an imperative approach before translation into the pons region that may cause significant brain damage to animals and is therefore in line with the 3Rs framework for the ethical use of animals in research. Likewise, we previously investigated the distribution of other types of NPs in the normal gray and white matter after CED infusion into the striatum/white matter of Wistar rats and pigs.[21,66] The importance of the spheroid model is not to be underestimated, since the distribution in a genetically modified rodent tumor may be very different from a human, and there are very few human lines suitable for orthotopic xenografts that can accurately recapitulate patient tumors. Further preclinical experiments in rat DIPG models are planned to assess the survival benefits and toxicity profile of these N3P nano-constructs.

4. CONCLUSIONS

The nanoformulations of TMZ/N3P were reproducibly developed via simple and nondisruptive methods, i.e., without any derivatization, heat denaturation, or cross-linking step, and achieved favorable drug loading and stability. In addition, the small size (<100 nm) and negative surface charge of AFt and Lip NPs were utilized to particularly enhance the CED distribution and penetration *in vivo*. Both TMZ- and N3P-loaded NPs exhibited a sustained release profile with a significantly superior dose–response effect of TMZ/N3P NPs against 2D or 3D spheroid models of MGMT$^+$ or MMR-deficient DIPGs as compared to native drugs. AFt nanocage delivery specifically contributed to TMZ chemosensitization in resistant DIPG cell lines likely by TfR1-mediated uptake and delivery of a larger dose of TMZ to the intracellular site of action that exhausts and depletes MGMT. Moreover, AFt NPs'

https://doi.org/10.1021/acsami.1c04164
ACS Appl. Mater. Interfaces XXXX, XXX, XXX–XXX

CED distribution analysis offered substantial enhancement over free ^{89}Zr radionuclide (Supplementary Figure S11) in terms of tissue retention and sustained distribution within the brain parenchyma following a single infusion. These data, in common with previous reports for nanoliposomes' brain distribution,[38,43] suggest that AFt- or Lip-mediated CED of N3P may overcome challenges faced with treatment of TMZ-resistant DIPGs or other brain tumors, circumventing its poor solubility, fast degradation kinetics, and BBB-restricted delivery. Overall, by combining CED and the greater half-life of these drugs in the NPs, the administrated dose and systemic toxicities are likely to be minimized. Future work in preclinical models will lead to a fundamental understanding of the survival benefit and pharmacokinetics of these formulations. These long-acting NPs can also be tailored to incorporate a variety of therapeutic agents that are similarly unstable or insoluble in physiological conditions for broad treatment of intracranial diseases.

■ ASSOCIATED CONTENT

Supporting Information

The Supporting Information is available free of charge at https://pubs.acs.org/doi/10.1021/acsami.1c04164.

Detailed Experimental Section; ^{1}H NMR chemical shifts (δ) and changes ($\Delta\delta$) of free TMZ, N3P, or SBE-β-CD protons; particle size, polydispersity index (PdI), and surface charge of NPs; ^{1}H NMR spectra of TMZ, SBE-β-CD, and CD-TMZ complex and N3P, SBE-β-CD, and CD-N3P complex; cytotoxic effects of TMZ/N3P, CD-TMZ/N3P complexes, or TMZ/N3P-loaded AFt or Lip NPs in MGMT^{-} DIPG-XIX and SF7761 cell lines; safety profile of control NPs in various 3D DIPG spheroids; representative phase-contrast and H&E staining images of DIPG spheroids; comparison of 2D vs 3D sensitivity of DIPG-IV and -XIX cultures toward free N3P or N3P-loaded NPs; growth inhibitory effects of 50 μM N3P, CD-N3P complex, or N3P-loaded AFt or Lip NPs in various 3D DIPG spheroids; growth inhibitory effects of 400 μM TMZ, CD-TMZ complex, or TMZ-loaded AFt or Lip NPs in various 3D DIPG spheroids; representative images of DIPG-IV, DIPG-VI, DIPG-XIX, and SF7761 spheroids obtained before (day 0) and 4 days post-treatment with 400 μM TMZ formulations or controls; representative radio-TLC scans of free ^{89}Zr in comparison to ^{89}Zr-DFO-AFt reaction mixture with 100% radiochemical purity; analytical radio-HPLC chromatograms of ^{89}Zr-Oxalate, ^{89}Zr-DFO, ^{89}Zr-DFO-AFt, and ^{89}Zr-DFO-Lip NPs; representative *in vivo* PET/CT and PET images (PDF)

■ AUTHOR INFORMATION

Corresponding Author

Beth Coyle − *Children's Brain Tumour Research Centre, School of Medicine, Biodiscovery Institute, University of Nottingham, Nottingham, Nottinghamshire NG7 2RD, United Kingdom;* orcid.org/0000-0003-2957-1862; Phone: +441158230719; Email: beth.coyle@nottingham.ac.uk; Fax: +441158230696

Authors

Vahid Heravi Shargh − *Children's Brain Tumour Research Centre, School of Medicine, Biodiscovery Institute, University of Nottingham, Nottingham, Nottinghamshire NG7 2RD, United Kingdom;* orcid.org/0000-0002-6388-9877

Jeni Luckett − *School of Life Sciences, Biodiscovery Institute, University of Nottingham, Nottingham, Nottinghamshire NG7 2RD, United Kingdom*

Kaouthar Bouzinab − *School of Pharmacy, Biodiscovery Institute, University of Nottingham, Nottingham, Nottinghamshire NG7 2RD, United Kingdom*

Stephen Paisey − *Wales Research and Diagnostic PET Imaging Centre, School of Medicine, Cardiff University, Cardiff CF14 4XN, United Kingdom;* orcid.org/0000-0002-2274-3708

Lyudmila Turyanska − *Faculty of Engineering, University of Nottingham, Nottingham, Nottinghamshire NG7 2RD, United Kingdom;* orcid.org/0000-0002-9552-6501

William G. B. Singleton − *Department of Paediatric Neurosurgery, Bristol Royal Hospital for Children, Bristol BS2 8BJ, United Kingdom; Translational Health Sciences, Bristol Medical School, Faculty of Health Sciences, University of Bristol, Bristol BS8 1TD, United Kingdom*

Stephen Lowis − *Department of Haematology and Oncology, Bristol Royal Hospital for Children, Bristol BS2 8BJ, United Kingdom*

Pavel Gershkovich − *School of Pharmacy, Biodiscovery Institute, University of Nottingham, Nottingham, Nottinghamshire NG7 2RD, United Kingdom;* orcid.org/0000-0003-3136-0933

Tracey D. Bradshaw − *School of Pharmacy, Biodiscovery Institute, University of Nottingham, Nottingham, Nottinghamshire NG7 2RD, United Kingdom;* orcid.org/0000-0001-8451-5092

Malcolm F. G. Stevens − *School of Pharmacy, Biodiscovery Institute, University of Nottingham, Nottingham, Nottinghamshire NG7 2RD, United Kingdom*

Alison Bienemann − *Translational Health Sciences, Bristol Medical School, Faculty of Health Sciences, University of Bristol, Bristol BS8 1TD, United Kingdom*

Complete contact information is available at: https://pubs.acs.org/10.1021/acsami.1c04164

Author Contributions

V.H.S. carried out the experimental design and acquisition of data/analysis and drafted the manuscript under the supervision of B.C. All *in vivo* experiments were undertaken by J.L. and A.B., who contributed significantly to the analysis of this data. S.P. participated in the radiolabeling of NPs and the corresponding analysis. All other authors were involved in project planning, contributed to editing the manuscript, and have given approval to the final version of the manuscript.

Funding

This work was supported by grant 16-228 from the Children with Cancer UK (awarded to B.C.) and the EPSRC grant EP/L01646X/1 (awarded to K.B.).

Notes

The authors declare no competing financial interest.

■ ACKNOWLEDGMENTS

The authors thank the Nanoscale and Microscale Research Centre (nmRC) for providing access to instrumentation and Mrs. Nicola Weston for technical assistance in acquiring the TEM images.

REFERENCES

(1) Cooney, T. M.; et al. Diffuse midline glioma: review of epigenetics. *J. Neuro-Oncol.* **2020**, *150* (1), 27−34.
(2) Gwak, H. S.; Park, H. J. Developing chemotherapy for diffuse pontine intrinsic gliomas (DIPG). *Crit Rev. Oncol Hematol* **2017**, *120*, 111−119.
(3) Abe, H.; Natsumeda, M.; Okada, M.; Watanabe, J.; Tsukamoto, Y.; Kanemaru, Y.; Yoshimura, J.; Oishi, M.; Hashizume, R.; Kakita, A.; Fujii, Y.; et al. MGMT Expression Contributes to Temozolomide Resistance in H3K27M-Mutant Diffuse Midline Gliomas. *Front. Oncol.* **2020**, *9*, 1568−1568.
(4) Higuchi, F.; et al. Restoration of Temozolomide Sensitivity by PARP Inhibitors in Mismatch Repair Deficient Glioblastoma is Independent of Base Excision Repair. *Clin. Cancer Res.* **2020**, *26* (7), 1690−1699.
(5) Zhang, J.; et al. N3-Substituted Temozolomide Analogs Overcome Methylguanine-DNA Methyltransferase and Mismatch Repair Precipitating Apoptotic and Autophagic Cancer Cell Death. *Oncology* **2015**, *88* (1), 28−48.
(6) Cousin, D.; et al. Antitumor imidazo[5,1-d]-1,2,3,5-tetrazines: compounds modified at the 3-position overcome resistance in human glioblastoma cell lines. *MedChemComm* **2016**, *7* (12), 2332−2343.
(7) Bouzinab, K.; et al. In search of effective therapies to overcome resistance to Temozolomide in brain tumours. *Cancer Drug Resist.* **2019**, *2*, 1018−1031.
(8) Arvanitis, C. D.; Ferraro, G. B.; Jain, R. K. The blood-brain barrier and blood-tumour barrier in brain tumours and metastases. *Nat. Rev. Cancer* **2020**, *20* (1), 26−41.
(9) Munoz, J. L.; et al. Temozolomide competes for P-glycoprotein and contributes to chemoresistance in glioblastoma cells. *Cancer Lett.* **2015**, *367* (1), 69−75.
(10) de Gooijer, M. C.; et al. Improved Brain Penetration and Antitumor Efficacy of Temozolomide by Inhibition of ABCB1 and ABCG2. *Neoplasia* **2018**, *20* (7), 710−720.
(11) Groothuis, D. R. The blood-brain and blood-tumor barriers: a review of strategies for increasing drug delivery. *Neuro Oncol.* **2000**, *2* (1), 45−59.
(12) Singhal, N.; Selva-Nayagam, S.; Brown, M. P. Prolonged and severe myelosuppression in two patients after low-dose Temozolomide treatment- case study and review of literature. *J. Neuro-Oncol.* **2007**, *85* (2), 229−230.
(13) Trinh, V. A.; Patel, S. P.; Hwu, W. J. The safety of Temozolomide in the treatment of malignancies. *Expert Opin. Drug Saf.* **2009**, *8* (4), 493−499.
(14) Stine, C. A.; Munson, J. M. Convection-Enhanced Delivery: Connection to and Impact of Interstitial Fluid Flow. *Front. Oncol.* **2019**, *9*, 966.
(15) Yang, W.; et al. Convection enhanced delivery of carboplatin in combination with radiotherapy for the treatment of brain tumors. *J. Neuro-Oncol.* **2011**, *101* (3), 379−390.
(16) Allard, E.; Passirani, C.; Benoit, J. P. Convection-enhanced delivery of nanocarriers for the treatment of brain tumors. *Biomaterials* **2009**, *30* (12), 2302−2318.
(17) El-Khouly, F. E.; van Vuurden, D. G.; Stroink, T.; Hulleman, E.; Kaspers, G. J. L.; Hendrikse, N. H.; Veldhuijzen van Zanten, S. E. M.; et al. Effective Drug Delivery in Diffuse Intrinsic Pontine Glioma: A Theoretical Model to Identify Potential Candidates. *Front. Oncol.* **2017**, *7*, 254.
(18) McCrorie, P.; et al. Biomedical engineering approaches to enhance therapeutic delivery for malignant glioma. *J. Controlled Release* **2020**, *328*, 917−931.
(19) Yeini, E.; et al. Targeting Glioblastoma: Advances in Drug Delivery and Novel Therapeutic Approaches. *Adv. Ther* **2021**, *4*, 2000124.
(20) Arshad, A.; et al. Convection-Enhanced Delivery of Carboplatin PLGA Nanoparticles for the Treatment of Glioblastoma. *PLoS One* **2015**, *10* (7), No. e0132266.
(21) Singleton, W. G.; et al. Convection enhanced delivery of panobinostat (LBH589)-loaded pluronic nano-micelles prolongs survival in the F98 rat glioma model. *Int. J. Nanomed.* **2017**, *12*, 1385−1399.
(22) Belletti, D.; et al. Protein cage nanostructure as drug delivery system: magnifying glass on apoferritin. *Expert Opin. Drug Delivery* **2017**, *14* (7), 825−840.
(23) Luo, Y.; et al. Hyaluronic acid-conjugated apoferritin nanocages for lung cancer targeted drug delivery. *Biomater. Sci.* **2015**, *3* (10), 1386−1394.
(24) Ma-Ham, A.; et al. Apoferritin-based nanomedicine platform for drug delivery: equilibrium binding study of daunomycin with DNA. *J. Mater. Chem.* **2011**, *21* (24), 8700−8708.
(25) Santos, A. C.; et al. Cyclodextrin-based delivery systems for in vivo-tested anticancer therapies. *Drug Delivery Transl. Res.* **2021**, *11* (1), 49−71.
(26) Zappacosta, R.; et al. Effect of the Incorporation of Functionalized Cyclodextrins in the Liposomal Bilayer. *Molecules* **2019**, *24* (7), 1387.
(27) Lin, E. Y.; et al. Liposome Consolidated with Cyclodextrin Provides Prolonged Drug Retention Resulting in Increased Drug Bioavailability in Brain. *Int. J. Mol. Sci.* **2020**, *21* (12), 4408.
(28) Cui, J.; et al. Development of pegylated liposomal vincristine using novel sulfobutyl ether cyclodextrin gradient: is improved drug retention sufficient to surpass DSPE-PEG-induced drug leakage? *J. Pharm. Sci.* **2011**, *100* (7), 2835−2848.
(29) Celia, C.; et al. Physicochemical properties of inclusion complexes of highly soluble β-cyclodextrins with highly hydrophobic testosterone propionate. *Int. J. Pharm.* **2017**, *534* (1−2), 316−324.
(30) Bouzinab, K.; et al. Delivery of Temozolomide and N3-Propargyl Analog to Brain Tumors Using an Apoferritin Nanocage. *ACS Appl. Mater. Interfaces* **2020**, *12* (11), 12609−12617.
(31) Shargh, V. H.; Hondermarck, H.; Liang, M. Albumin hybrid nanoparticles loaded with tyrosine kinase A inhibitor GNF-5837 for targeted inhibition of breast cancer cell growth and invasion. *Int. J. Pharm.* **2016**, *515* (1−2), 527−534.
(32) Chen, J.; et al. Delivery of fluorescent-labeled cyclodextrin by liposomes: role of transferrin modification and phosphatidylcholine composition. *J. Liposome Res.* **2017**, *27* (1), 21−31.
(33) Zhai, M.; et al. Glioma targeting peptide modified apoferritin nanocage. *Drug Delivery* **2018**, *25* (1), 1013−1024.
(34) Watson, H. A.; Durairaj, R. R. P.; Ohme, J.; Alatsatianos, M.; Almutairi, H.; Mohammed, R. N.; Vigar, M.; Reed, S. G.; Paisey, S. J.; Marshall, C.; Gallimore, A.; Ager, A.; et al. L-Selectin Enhanced T Cells Improve the Efficacy of Cancer Immunotherapy. *Front. Immunol.* **2019**, *10*, 1321.
(35) Bradford, M. M. A rapid and sensitive method for the quantitation of microgram quantities of protein utilizing the principle of protein-dye binding. *Anal. Biochem.* **1976**, *72*, 248−254.
(36) Li, X.; et al. Enhanced Copper-Temozolomide Interactions by Protein for Chemotherapy against Glioblastoma Multiforme. *ACS Appl. Mater. Interfaces* **2019**, *11* (45), 41935−41945.
(37) Breen, A. F.; et al. Development of novel apoferritin formulations for antitumour benzothiazoles. *Cancer Rep* **2019**, *2* (4), No. e1155.
(38) Nordling-David, M. M.; et al. Liposomal Temozolomide drug delivery using convection enhanced delivery. *J. Controlled Release* **2017**, *261*, 138−146.
(39) Kirpotin, D.; et al. Sterically Stabilized Anti-HER2 Immunoliposomes: Design and Targeting to Human Breast Cancer Cells in Vitro. *Biochemistry* **1997**, *36* (1), 66−75.
(40) Maja, L.; Željko, K.; Mateja, P. Sustainable technologies for liposome preparation. *J. Supercrit. Fluids* **2020**, *165*, 104984.
(41) Torchilin, V. Antibody-modified liposomes for cancer chemotherapy. *Expert Opin. Drug Delivery* **2008**, *5* (9), 1003−1025.
(42) Szoka, F; Papahadjopoulos, D Comparative Properties and Methods of Preparation of Lipid Vesicles (Liposomes). *Annu. Rev. Biophys. Bioeng.* **1980**, *9* (1), 467−508.
(43) MacKay, J. A.; Deen, D. F.; Szoka, F. C., Jr. Distribution in brain of liposomes after convection enhanced delivery; modulation by

https://doi.org/10.1021/acsami.1c04164
ACS Appl. Mater. Interfaces XXXX, XXX, XXX−XXX

particle charge, particle diameter, and presence of steric coating. *Brain Res.* **2005**, *1035* (2), 139−153.
(44) Zhou, J.; et al. Highly penetrative, drug-loaded nanocarriers improve treatment of glioblastoma. *Proc. Natl. Acad. Sci. U. S. A.* **2013**, *110* (29), 11751−11756.
(45) Nance, E. A.; et al. A dense poly(ethylene glycol) coating improves penetration of large polymeric nanoparticles within brain tissue. *Sci. Transl. Med.* **2012**, *4* (149), 149ra119.
(46) Chen, E. M.; et al. Biodegradable PEG-poly(ω-pentadecalactone-co-p-dioxanone) nanoparticles for enhanced and sustained drug delivery to treat brain tumors. *Biomaterials* **2018**, *178*, 193−203.
(47) Noble, C. O.; et al. Novel nanoliposomal CPT-11 infused by convection-enhanced delivery in intracranial tumors: pharmacology and efficacy. *Cancer Res.* **2006**, *66* (5), 2801−2806.
(48) Saito, R.; et al. Convection-enhanced delivery of Ls-TPT enables an effective, continuous, low-dose chemotherapy against malignant glioma xenograft model. *Neuro Oncol* **2006**, *8* (3), 205−214.
(49) Kim, M.; et al. pH-dependent structures of ferritin and apoferritin in solution: disassembly and reassembly. *Biomacromolecules* **2011**, *12* (5), 1629−1640.
(50) Kuruppu, A. I.; et al. An Apoferritin-based Drug Delivery System for the Tyrosine Kinase Inhibitor Gefitinib. *Adv. Healthcare Mater.* **2015**, *4* (18), 2816−2821.
(51) Huang, Z.; London, E. Effect of Cyclodextrin and Membrane Lipid Structure upon Cyclodextrin-Lipid Interaction. *Langmuir* **2013**, *29* (47), 14631−14638.
(52) Kang, J. H.; Jang, W. Y.; Ko, Y. T. The Effect of Surface Charges on the Cellular Uptake of Liposomes Investigated by Live Cell Imaging. *Pharm. Res.* **2017**, *34* (4), 704−717.
(53) Yang, Y.; et al. Camptothecin-Polysaccharide Co-assembly and Its Controlled Release. *Bioconjugate Chem.* **2016**, *27* (12), 2834−2838.
(54) Fu, W.; et al. Enhanced Efficacy of Temozolomide Loaded by a Tetrahedral Framework DNA Nanoparticle in the Therapy for Glioblastoma. *ACS Appl. Mater. Interfaces* **2019**, *11* (43), 39525−39533.
(55) Fang, C.; et al. Temozolomide nanoparticles for targeted glioblastoma therapy. *ACS Appl. Mater. Interfaces* **2015**, *7* (12), 6674−6682.
(56) Kumari, S.; Ahsan, S. M.; Kumar, J. M.; Kondapi, A. K.; Rao, N. M.; et al. Overcoming blood brain barrier with a dual purpose Temozolomide loaded Lactoferrin nanoparticles for combating glioma (SERP-17−12433). *Sci. Rep.* **2017**, *7* (1), 6602.
(57) Appel, E. A.; et al. Enhanced stability and activity of Temozolomide in primary glioblastoma multiforme cells with cucurbit[n]uril. *Chem. Commun. (Cambridge, U. K.)* **2012**, *48* (79), 9843−9845.
(58) Arcella, A.; et al. Brain Targeting by Liposome-Biomolecular Corona Boosts Anticancer Efficacy of Temozolomide in Glioblastoma Cells. *ACS Chem. Neurosci.* **2018**, *9* (12), 3166−3174.
(59) Curtis, L. T.; et al. An interdisciplinary computational/experimental approach to evaluate drug-loaded gold nanoparticle tumor cytotoxicity. *Nanomedicine (London, U. K.)* **2016**, *11* (3), 197−216.
(60) Melissaridou, S.; Wiechec, E.; Magan, M.; Jain, M. V.; Chung, M. K.; Farnebo, L.; Roberg, K.; et al. The effect of 2D and 3D cell cultures on treatment response, EMT profile and stem cell features in head and neck cancer. *Cancer Cell Int.* **2019**, *19* (1), 16.
(61) Breslin, S.; O'Driscoll, L. The relevance of using 3D cell cultures, in addition to 2D monolayer cultures, when evaluating breast cancer drug sensitivity and resistance. *Oncotarget* **2016**, *7*, 45745−45756.
(62) Imamura, Y.; et al. Comparison of 2D- and 3D-culture models as drug-testing platforms in breast cancer. *Oncol. Rep.* **2015**, *33* (4), 1837−1843.
(63) Nunes, A. S.; et al. 3D tumor spheroids as in vitro models to mimic in vivo human solid tumors resistance to therapeutic drugs. *Biotechnol. Bioeng.* **2019**, *116* (1), 206−226.
(64) Shen, Y.; Li, X.; Dong, D.; Zhang, B.; Xue, Y.; Shang, P.; et al. Transferrin receptor 1 in cancer: a new sight for cancer therapy. *Am. J. Cancer Res.* **2018**, *8* (6), 916−931.
(65) Sirianni, R. W.; et al. Radiolabeling of poly(lactic-co-glycolic acid) (PLGA) nanoparticles with biotinylated F-18 prosthetic groups and imaging of their delivery to the brain with positron emission tomography. *Bioconjugate Chem.* **2014**, *25* (12), 2157−2165.
(66) Singleton, W. G. B.; et al. The distribution, clearance, and brainstem toxicity of panobinostat administered by convection-enhanced delivery. *J. Neurosurg Pediatr* **2018**, *22* (3), 288−296.

https://doi.org/10.1021/acsami.1c04164
ACS Appl. Mater. Interfaces XXXX, XXX, XXX−XXX